catalysts

MDPI

Article

One-Pot Synthesis of Structurally Tunable Ag@Fe_3O_4 Nanoreactors for Ultra-Efficient and Magnetically Recyclable Reduction of 4-Nitrophenol

Sihui Song [1], Chunting Li [2], Sadaf Mutahir [1], Muhammad Asim Khan [1,*] and Feng Yan [1,*]

[1] School of Chemistry & Chemical Engineering, Linyi University, Linyi 276000, China; 240703001544@lyu.edu.cn (S.S.); sadafmutahir@lyu.edu.cn (S.M.)
[2] School of Materials Science & Engineering, Linyi University, Linyi 276000, China; 250856001809@lyu.edu.cn
* Correspondence: khanabdali@lyu.edu.cn (M.A.K.); yanfeng@lyu.edu.cn (F.Y.)

Abstract

The catalytic reduction of toxic 4-Nitrophenol (4-NP) to valuable 4-aminophenol is highly important for environmental remediation. However, developing catalysts with high activity, good recyclability, and facile preparation remains challenging. Herein, Ag@Fe_3O_4 nanocomposites were controllably synthesized with a facile one-pot polyol method. By varying the Ag:Fe precursor ratio, the structure could be tuned from dense and porous core-shell to Janus architectures. The porous Ag@Fe_3O_4 nanoreactors (Ag:Fe-0.4) exhibited exceptional catalytic performance, achieving complete 4-NP reduction within 75 s, with an apparent rate constant (k) of 6.29 × 10^{-2} s^{-1}, a normalized rate constant (k_n) of 3742 s^{-1} $mmol^{-1}$, and a TOF value of 1042 h^{-1}. XPS results verified that the excellent activity originated from the porous structure and interfacial charge transfer from Ag to Fe_3O_4. The catalysts showed super-paramagnetism and could be reused for at least eight cycles with >95% conversion retained. It also displayed high efficiency in reducing diverse nitroaromatics and in natural water. This work highlights the significance of structural and electronic modulation, providing a scalable strategy for magnetically recyclable catalysts toward environmental remediation and heterogeneous catalysis.

Keywords: Ag@Fe_3O_4 nanocomposites; 4-nitrophenol reduction; porous nanoreactors; one-pot synthesis; charge transfer

1. Introduction

The catalytic reduction of 4-Nitrophenol (4-NP), a prevalent and toxic industrial wastewater pollutant, into valuable p-aminophenol (4-AP) represents a critical model reaction for both environmental protection and green chemical synthesis [1–5]. The severity of 4-nitrophenol contamination is underscored by its regulatory classification by multiple international agencies. The U.S. Environmental Protection Agency (EPA) lists 4-NP as a "priority pollutant" under the Clean Water Act, while the European Chemicals Agency (ECHA) designates it as a "Substance of Very High Concern (SVHC)" due to its endocrine-disrupting, carcinogenic, and mutagenic risks [6]. Global annual release of 4-NP into natural water bodies is estimated at approximately 10,000–15,000 tons, primarily originating from industrial effluents of pesticide, dye, pharmaceutical, and explosive manufacturing processes [7]. The significance of this transformation is underscored by the stringent classification of 4-NP as a priority pollutant by regulatory bodies like the U.S. Environmental Protection Agency (EPA), a designation reserved for compounds posing significant risks to human health

Academic Editor: Alain Roucoux

Received: 29 March 2026
Revised: 3 May 2026
Accepted: 9 May 2026
Published: 11 May 2026

and ecological balance [8–10]. The detrimental impact of 4-NP stems from its stability, its solubility, and its role as a potent endocrine disruptor, which can interfere with hormonal functions and lead to long-term carcinogenic and mutagenic effects [8,11,12]. Consequently, the development of efficient and sustainable technologies for its removal is not merely an academic pursuit but a pressing industrial and environmental necessity [13].

Several remediation strategies have been explored to mitigate 4-NP contamination, but each suffers from inherent limitations. Physical adsorption using activated carbon or clays effectively removes 4-NP but generates secondary solid waste and requires energy-intensive regeneration [14]. Advanced oxidation processes (AOPs) achieve complete mineralization but demand high energy input, chemical oxidants, and may form toxic byproducts [15]. Electrochemical treatment avoids chemical addition yet faces electrode fouling, high operational costs, and poor scalability [11]. Biological degradation is environmentally friendly but exhibits very slow kinetics, low tolerance to high 4-NP concentrations, and prolonged acclimation periods [16–18]. In contrast, catalytic hydrogenation of 4-NP to 4-AP using $NaBH_4$ as a reductant presents a uniquely "green" and atom-efficient pathway [19]. This process accomplishes dual objectives: it detoxifies a hazardous pollutant and concurrently upgrades it into a valuable commodity chemical. Moreover, 4-AP is a critical precursor in the manufacturing of analgesic and antipyretic drugs (e.g., paracetamol), corrosion inhibitors, photographic developers, and hair-dyeing agents, enhancing the economic viability of the remediation process [20–22].

The efficacy of this reduction reaction is intrinsically linked to the performance of the catalyst, driving extensive research into noble metal nanocatalysts [23]. Materials based on Au, Pt, Pd, and Ag have been at the forefront due to their exceptional surface reactivity and superior ability to facilitate electron transfer from the borohydride donor (BH_4^-) to the 4-NP acceptor [24–35]. Beyond mere composition, the field has increasingly recognized that catalytic performance is profoundly governed by nanoscale structural parameters. Seminal works have demonstrated that precise control over particle size, morphology, and exposed crystal facets can dramatically enhance activity and selectivity [27–29]. For instance, Ruditskiy et al. illustrated how Ag nanocubes enclosed by (100) facets exhibit distinctive catalytic properties compared to their spherical counterparts [36]. Similarly, the construction of complex architectures like Au-based nanocages and nanoboxes by Xia and others has revealed how geometric design dictates catalytic efficiency [37,38]. Among these noble metals, Ag nanomaterials have garnered significant interest as a cost-effective and highly active alternative, offering a compelling combination of tunable plasmonic properties, ease of morphological manipulation, and high intrinsic activity for 4-NP reduction [32,33,37]. Despite these compelling advantages, the practical deployment of Ag-based nanocatalysts is hampered by two inherent and persistent limitations. First, their high surface energy predisposes them to irreversible aggregation and Oswald ripening during catalytic cycles, leading to a precipitous loss of active surface area and a corresponding decline in performance [22]. Second, more critically from an application standpoint, their nanoscale dimensions make their separation and recovery from the reaction mixture exceptionally challenging [22]. Conventional separation techniques like centrifugation or filtration are often inefficient, time-consuming, and costly at an industrial scale, thereby increasing operational expenses and posing risks of secondary environmental release through catalyst leaching.

The integration of magnetic nanoparticles, particularly superparamagnetic Fe_3O_4, as a catalyst support has emerged as a highly attractive and seemingly elegant strategy to address the separation dilemma [39–41]. This approach enables the facile, rapid, and efficient recovery of catalysts using an external magnet, promising seamless recyclability and reusability. However, this promising solution often introduces new complexities and a

critical performance trade-off. Many reported synthesis routes for such magnetic composites are multi-step, are time-consuming, and require sophisticated surface functionalization or ligand exchange, which can hinder scalability [30,42,43]. More fundamentally, a pervasive challenge exists in balancing separability with catalytic activity. The formation of a dense, thick Fe_3O_4 shell around the noble metal core, while beneficial for ensuring strong magnetism and stability, can physically block reactant molecules from accessing the active catalytic sites [44–46]. This mass-transfer limitation results in composite materials that are easily recyclable but exhibit disappointingly low activity and slow reaction kinetics, effectively negating the primary purpose of using a highly active precious metal. For example, while traditional core-shell structures provide excellent protection against aggregation, their non-porous nature often leads to severely limited performance [45–49].

Therefore, the design of a catalyst that simultaneously possesses unimpeded accessibility to active sites, robust magnetic recyclability, and a simple, scalable synthesis route remains an outstanding and critically important challenge in the field. Herein, we present a strategic design to overcome these conflicting demands through a facile one-pot polyol synthesis of structurally tunable Ag@Fe_3O_4 nanoreactors, as shown in Figure 1. We hypothesized that by carefully controlling the nucleation and growth kinetics through the Ag:Fe precursor ratio, we could engineer diverse interfacial architectures from dense core-shell to porous core-shell and Janus configurations from a single, scalable synthetic platform. We posited that a porous Fe_3O_4 shell would serve a dual function: acting as a protective, magnetically responsive matrix to prevent Ag aggregation while remaining permeable to reactant molecules and participating in interfacial charge transfer to electronically modulate the Ag surface, thereby enhancing its intrinsic activity. In this work, we demonstrate that the optimized porous Ag@Fe_3O_4 nanoreactors (Ag:Fe-0.4:1) exhibit exceptional catalytic performance, reducing 4-NP to 4-AP with a remarkable completion time of 75 s. This translates to an outstanding apparent rate constant of 6.29×10^{-2} s^{-1} and a record-high turnover frequency (TOF) of 1042 h^{-1}. Through X-ray photoelectron spectroscopy (XPS), we provide direct evidence of significant charge transfer from Ag to Fe_3O_4, which we identify as a key mechanistic factor for the accelerated kinetics. The robust nanocomposites exhibit super-paramagnetism, enabling rapid magnetic separation and reuse for at least eight consecutive cycles with no significant loss of activity, retaining over 95% conversion. Notably, the porous Ag@Fe_3O_4 magnetic nanoreactors maintained excellent catalytic performance in the reduction of nitroaromatics bearing different functional groups, as well as in natural aqueous solutions. This work establishes a versatile paradigm for designing efficient, durable, and practical nanocatalysts for environmental remediation and broader heterogeneous catalytic applications.

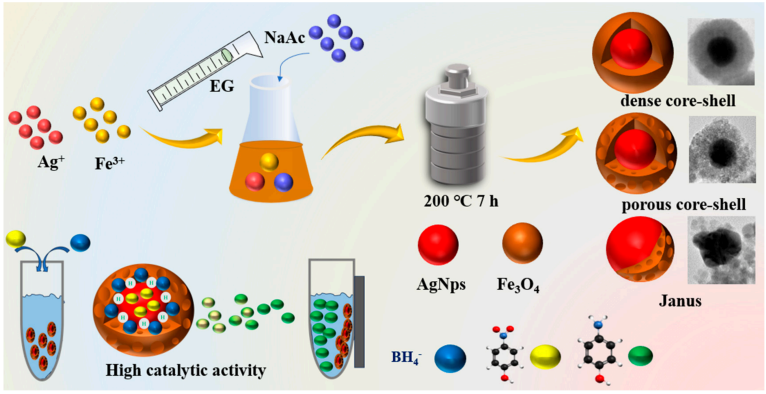

Figure 1. Schematic illustration of the synthesis of Ag/Fe_3O_4 magnetic nanocomposites with different structure and the reduction of 4-Nitrophenol to 4-Aminophenol.

2. Results and Discussion

2.1. Characterization of Ag/Fe_3O_4 Magnetic Nanocomposites

The Ag/Fe_3O_4 magnetic nanocomposites were successfully synthesized via a one-step polyol reduction process. The crystalline structure and phase purity of the as-prepared samples were first ascertained by XRD. As presented in Figure 2A, all diffraction patterns unambiguously confirm the co-existence of crystalline metallic silver (Ag^0) and magnetite (Fe_3O_4). The characteristic reflections observed at 2θ values of 38.13°, 44.37°, 64.55°, and 77.51° are readily indexed to the (111), (200), (220), and (311) lattice planes of face-centered cubic (fcc) Ag (JCPDS No. 04-0783) [41,50]. Concurrently, the distinct peaks at 30.22°, 35.53°, 43.23°, 53.67°, 57.16°, and 62.73° correspond perfectly to the (220), (311), (400), (422), (511), and (440) planes of the cubic spinel structure of Fe_3O_4 (JCPDS No. 19-0629) [41,50]. The absence of diffraction peaks attributable to impurities, such as Fe_2O_3 or Ag_2O, underscores the high phase purity of the synthesized nanocomposites. Furthermore, as anticipated, the relative intensity of the Ag diffraction peaks exhibits a systematic enhancement with increasing nominal Ag:Fe molar ratio, indicative of a greater volume fraction of the metallic silver phase within the composite structures.

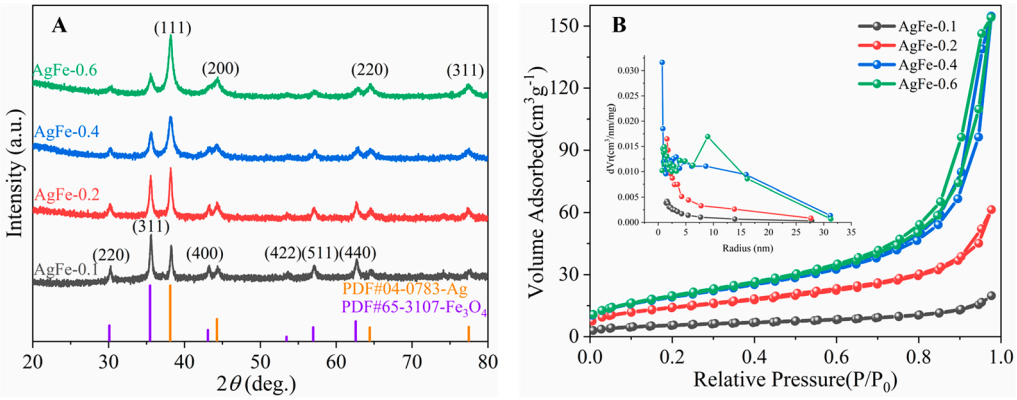

Figure 2. (**A**) XRD pattern of Ag/Fe_3O_4 magnetic nanocomposites with different structure, (**B**) N_2 adsorption–desorption isotherms of Ag/Fe_3O_4 magnetic nanocomposites. The inset in Figure (**B**) is pore diameter distributions of Ag/Fe_3O_4 magnetic nanocomposite.

The morphological and structural evolution of the Ag/Fe_3O_4 nanocomposites, as a direct function of the Ag:Fe precursor ratio, was elucidated through transmission electron microscopy (TEM) analysis. Representative micrographs in Figure 3 reveal a systematic architectural progression from dense core-shell to porous core-shell and finally to Janus structures. At the lowest Ag:Fe ratio (0.1:1, Figure 3A,E), the nanocomposites exhibit a classic, dense core-shell morphology. The distinct contrast, characterized by a dark, electron-dense Ag core and a lighter, electron-translucent Fe_3O_4 shell, arises from the significant difference in electron scattering cross-sections between the high-atomic-number Ag and the lower-atomic-number iron oxide. Statistical analysis (Figure S1A,E) confirms a well-defined structure with an Ag core diameter of 119.18 ± 29.65 nm, a total particle diameter of 310 ± 39.90 nm, and a corresponding dense Fe_3O_4 shell thickness of approximately 191 ± 36.60 nm. From SEM image (in Figure 4A), AgFe-0.1 nanocomposites also shows spherical structure with particle diameter of 310 nm.

This core-shell formation is governed by differential reduction kinetics in the polyol medium. The higher standard reduction potential of Ag^+/Ag^0 (+0.80 V vs. SHE) compared to Fe^{3+}/Fe^{2+} (+0.77 V vs. SHE) facilitates the preferential nucleation and growth of metallic Ag seeds at lower temperatures (~160 °C) [51]. These pre-formed Ag nanoparticles subsequently act as heterogeneous nucleation sites. We propose a synergistic mechanism where the Ag^0 surface catalyzes the reduction of Fe^{3+} to Fe^{2+}, which promotes the localized

precipitation and growth of a continuous, dense Fe_3O_4 shell in the presence of hydroxide ions from sodium acetate.

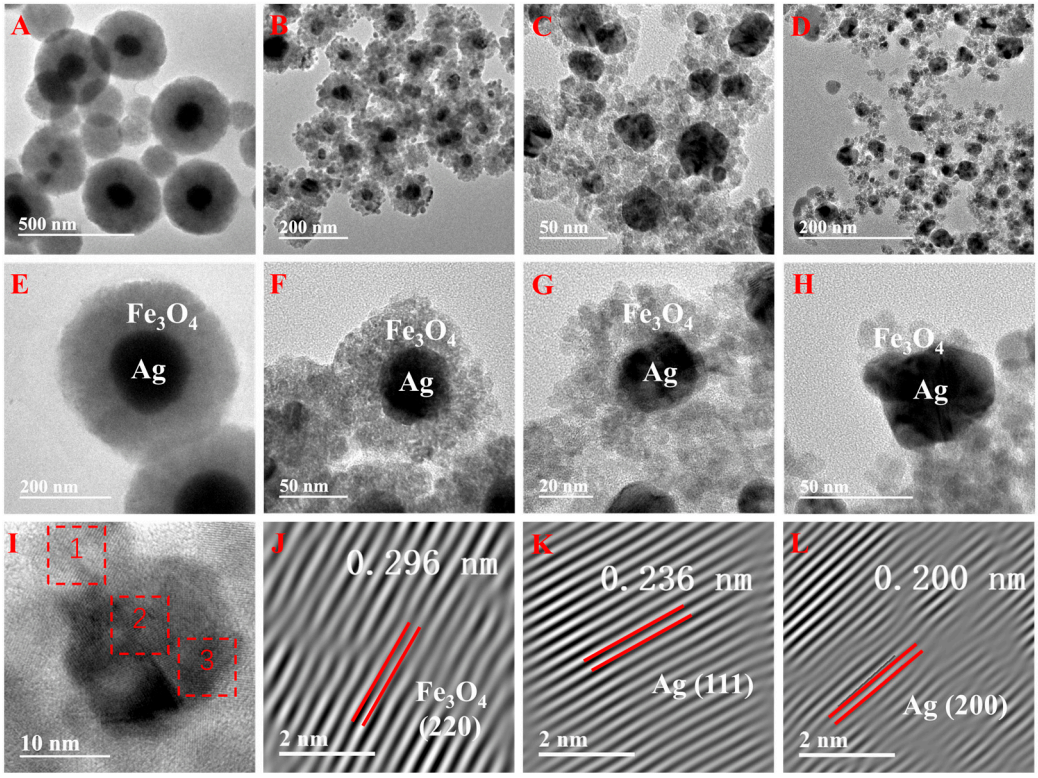

Figure 3. (**A**–**H**) TEM images of Ag/Fe_3O_4 magnetic nanocomposites with different structure: (**A**,**E**) AgFe-0.1, (**B**,**F**) AgFe-0.2, (**C**,**G**) AgFe-0.4, (**D**,**H**) AgFe-0.6. (**I**) HR-TEM images of AgFe-0.4 magnetic nanocomposites. (**J**–**L**) The corresponding inverse FFT images in Figure (**I**): (**J**) position 1, (**K**) position 2, and (**L**) position 3.

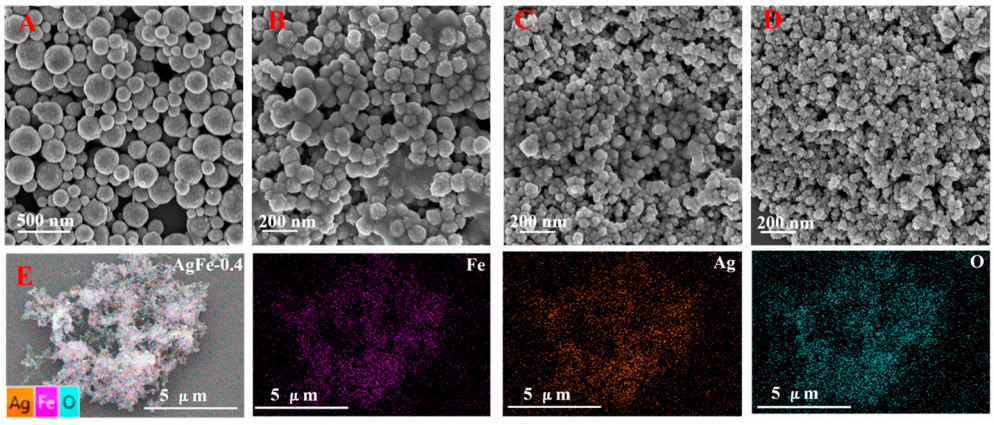

Figure 4. (**A**–**D**) SEM images of Ag/Fe_3O_4 magnetic nanocomposites with different structure: (**A**) AgFe-0.1, (**B**) AgFe-0.2, (**C**) AgFe-0.4, and (**D**) AgFe-0.6. (**E**) EDS elemental mappings of AgFe-0.4 magnetic nanocomposites.

Upon increasing the Ag:Fe ratio to 0.2:1 and 0.4:1, a fundamental morphological transition occurs. While a core-shell geometry is maintained (Figure 3B,C,F,G), the nanostructures undergo a significant size reduction and the Fe_3O_4 shell becomes porous. Particle size analysis (Figure S1B,C,F,G) shows the total diameter decreases to 105.79 ± 15.74 nm (Ag:Fe-0.2) and 51.64 ± 13.11 nm (Ag:Fe-0.4), with the Ag core diameter concurrently decreasing to 45.88 ± 11.43 nm and 24.07 ± 7.48 nm, respectively. Diameter decrease from Ag:Fe-0.1 to Ag:Fe-0.4 also proved by SEM images in Figure 4. This trend is a direct

consequence of the fixed Fe precursor concentration combined with increasing $AgNO_3$. The higher Ag^+ availability promotes a greater number of nucleation events, yielding a larger population of smaller Ag seeds. The limited iron precursor is then insufficient to form complete, dense shells over all available seed surfaces, resulting in the formation of a porous Fe_3O_4 matrix [52]. The N_2 adsorption–desorption isotherms of the magnetic composites were shown in Figure 2B, which exhibited the characteristic curves of porous materials. The BET surface area, pore volume, and pore size were obtained from the isotherms as shown in Figure 2B and Table S1, which confirmed a substantially larger specific surface area for the porous AgFe-0.4 nanocomposite compared to the dense-shell analogue. Ag:Fe-0.4 nanocomposites were characterized with SEM and EDX elemental mapping in Figures 4E and S2C.

HR-TEM of the optimized porous AgFe-0.4 nanocomposite (Figure 3I) confirms its high crystallinity. Lattice fringe analysis of the designated regions, supported by inverse Fast Fourier Transform (IFFT) images (Figure 3J–L), reveals distinct interplanar spacings of 0.296 nm, 0.236 nm, and 0.20 nm. These values correspond unambiguously to the (220) plane of Fe_3O_4, the (111) plane of Ag, and the (200) plane of Ag, respectively [53,54], confirming the intimate coexistence of both crystalline phases at the interface. At the highest Ag:Fe ratio of 0.6:1, the structural evolution culminates in a Janus morphology (Figure 3D,H). In this configuration, the Fe_3O_4 phase deposits asymmetrically, covering only a portion of the Ag seed surface. This occurs when the population of Ag seeds is maximized, and the limited iron species undergo preferential nucleation on specific facets or regions of the Ag seeds, resulting in the observed heterodimer structure. EDS (Figure S2) and quantitative analysis (Table 1) verify the co-localization of Ag and Fe in all architectures and confirm that the elemental composition shifts consistently with the nominal precursor ratios. The heterogeneous Ag/Fe_3O_4 nanocomposites with controlled morphology and nanostructure enables the tuning plasmonic resonance, shown in Figure S3 [55].

Table 1. The element percentages of Ag/Fe_3O_4 magnetic nanocomposites: (A) AgFe-0.1, (B) AgFe-0.2, (C) AgFe-0.4, and (D) AgFe-0.6.

Ag/Fe_3O_4 Magnetic Nanocomposite	**ICP**		**EDS**	
	Ag (Molar %)	**Fe (Molar %)**	**Ag (Molar %)**	**Fe (Molar %)**
AgFe-0.1	9.77	90.23	11.84	88.16
AgFe-0.2	16.45	83.55	18.99	81.01
AgFe-0.4	28.95	71.05	35.09	64.91
AgFe-0.6	39.44	60.56	44.14	55.86

XPS was employed to probe the surface chemical states and investigate the interfacial electronic interaction between Ag and Fe_3O_4. The survey spectra (Figure 5A) confirm the expected elemental composition. For the AgFe-0.1 and AgFe-0.2 nanocomposites, only Fe and O signals are detectable, indicating that the thick, dense Fe_3O_4 shell completely attenuates the photoelectrons from the underlying Ag core. In contrast, distinct Ag 3d peaks emerge in the spectra of the AgFe-0.4 and AgFe-0.6 nanocomposites, consistent with their porous and Janus structures, which expose the Ag domains to the surface. High-resolution analysis of the Ag 3d region (Figure 5B) reveals doublet peaks corresponding solely to metallic Ag^0 (Ag $3d_5/_2$ and Ag $3d_3/_2$), with no evidence of Ag^+ species. A critical trend is observed in the precise binding energy of the Ag $3d_5/_2$ peak. As the Ag content increases from the AgFe-0.2 to the AgFe-0.6 sample, the Ag $3d_5/_2$ binding energy undergoes a progressive negative shift, from 368.1 eV to 368.3 eV and finally to 368.15 eV [56]. This shift toward lower binding energy indicates an increase in electron density on the Ag atoms. Critical evidence for interfacial electronic coupling was derived from the Fe 2p spectra.

A systematic positive shift in the Fe 2p binding energy was observed, increasing from 710.85 eV for AgFe-0.2 to 711.35 eV for AgFe-0.6. This consistent increase is indicative of a decrease in electron density around the Fe species in Fe_3O_4. This phenomenon is attributed to a charge transfer effect, wherein electron density is donated from the metallic Ag seeds to the Fe_3O_4 shell at their interface [41,47]. The magnitude of this binding energy shift correlates with the Ag content, suggesting that a higher density of Ag seeds enhances the electronic interaction. Such interfacial charge transfer is known to modify the local electronic structure, which can significantly influence the catalytic and functional properties of the heterostructures [47].

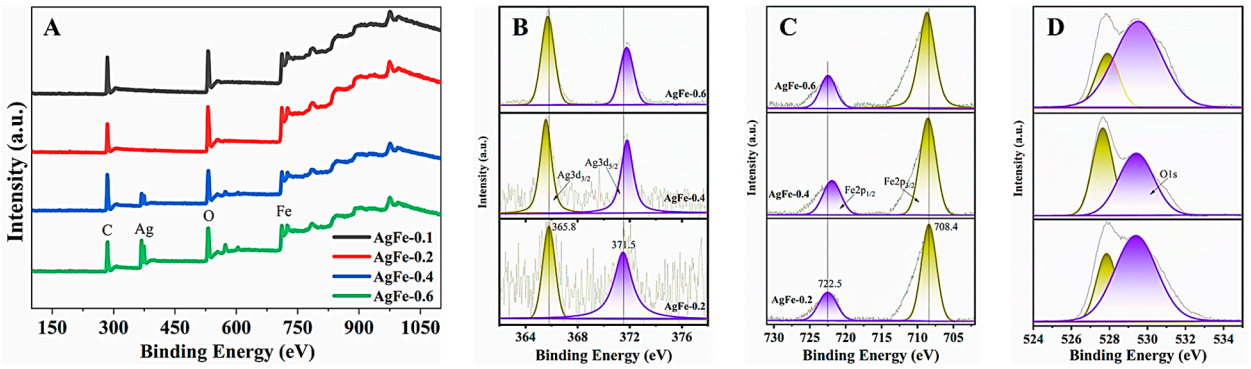

Figure 5. (**A**) XPS full spectra, (**B**) Ag 3d, (**C**) Fe 2p, and (**D**) O 2p of Ag/Fe_3O_4 magnetic nanocomposites.

2.2. Catalytic Performance of Ag/Fe_3O_4 Magnetic Nanocomposites

2.2.1. Catalytic Activity and the Role of Nanostructure

The catalytic efficacy of the Ag/Fe_3O_4 magnetic nanocomposites was evaluated using the benchmark reduction of 4-NP to 4-AP using $NaBH_4$ in aqueous solution. The reaction progress was monitored via UV-vis spectroscopy by tracking the decay of the 4-nitrophenolate ion absorbance at 400 nm (Figure 6A) [57,58]. Control experiments confirmed the reaction is negligible without a catalyst. A stark contrast in performance was observed among the different nanostructures. The dense AgFe-0.1 core-shell nanocomposite showed negligible activity, as the 400 nm peak intensity remained constant (Figure 6B). This is attributed to its non-porous Fe_3O_4 shell (Figure 3A,E), which physically blocks reactant access to the active Ag core. In contrast, the introduction of porous $Ag@Fe_3O_4$ nanocomposites (AgFe-0.2 and AgFe-0.4) resulted in a rapid decrease of the 400 nm peak, concomitant with the rise of a new peak at 300 nm corresponding to 4-AP (Figure 6A). This confirms the critical role of the porous morphology (Figure 3B,C,F,G), which facilitates mass transport, as further evidenced by their higher BET surface areas (Figure 2B).

2.2.2. Quantitative Kinetic Analysis

Given the significant excess of $NaBH_4$, its concentration remained effectively constant, allowing the reaction kinetics to be treated as pseudo-first-order with respect to 4-NP. The apparent rate constant k was therefore determined from the linear slope of a plot of $-\ln(A_t/A_0)$ versus time (Figure 6C), according to the integrated rate law:

$$-\ln(C_t/C_0) = -\ln(A_t/A_0) = kt$$

where C_0 and C_t represent the initial concentration and the concentration at time t, and A_0 and A_t are the absorbances at 400 nm at the initial state and at time t, respectively.

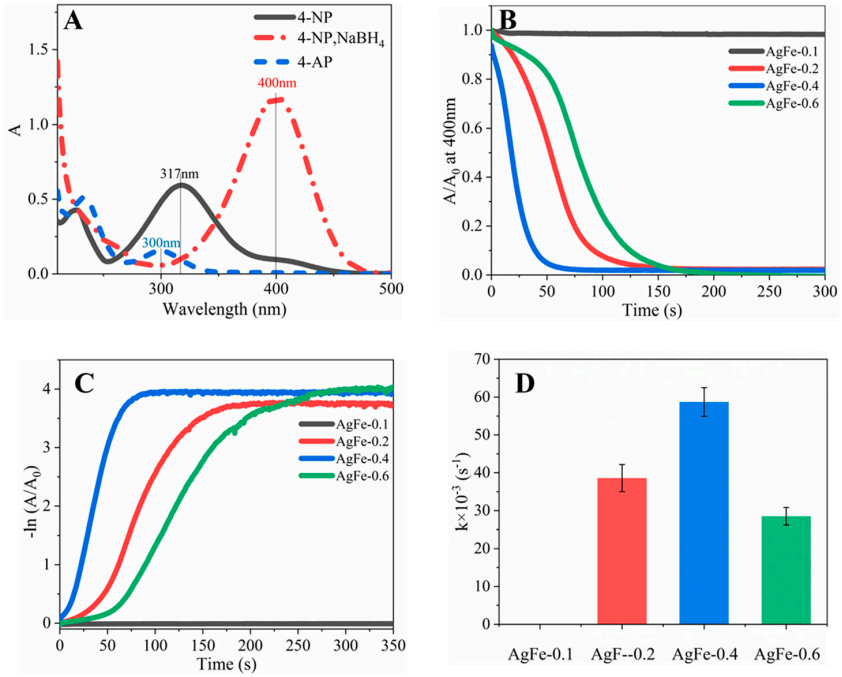

Figure 6. Catalytic performance of Ag/Fe_3O_4 magnetic nanocomposites for the reduction of 4-NP. (**A**) The adsorption spectra of 4-NP, 4-NP and $NaBH_4$ solution, and 4-AP. (**B**) Normalized A_t/A_0 at λ = 400 nm vs. reaction time for the reaction catalyzed by different nanocomposites. (**C**) Pseudo-first-order kinetic plots derived from the data in (**B**). (**D**) Bar chart of the apparent rate constant (k) calculated from the slopes in (**C**).

The AgFe-0.4 nanocomposite achieved complete conversion in just 75 s with a rate constant of 6.29×10^{-2} s^{-1}, significantly higher than that of AgFe-0.2 (4.06×10^{-2} s^{-1}) and AgFe-0.6 (3.08×10^{-2} s^{-1}). To enable a fair comparison of intrinsic activity, the normalized rate constant (k_n) and turnover frequency (TOF) were calculated. The AgFe-0.4 catalyst delivered outstanding values (k_n = 3742 s^{-1} $mmol^{-1}$; TOF = 1042 h^{-1}), which are competitive with, or superior to, other leading catalysts (Table 2).

Table 2. The comparison of catalytic performances of various nanocatalysts.

Catalysts	Catalyst (mg)	Reaction Time	k (s^{-1})	k_{nor} (s^{-1} $mmol^{-1}$)	TOF (h^{-1})	Ref.
AgFe-0.2	0.005	150 s	4.06×10^{-2}	4068	1133	This work
AgFe-0.4	0.005	75 s	6.29×10^{-2}	3742	1042	This work
AgFe-0.6	0.005	200 s	3.08×10^{-2}	1398	389	This work
Ag/PAM/PPy/GO	4	2.5 min	3.38×10^{-2}		60.24	[59]
Ag-Au-rGO	0.1	360 s	0.35×10^{-2}		152	[60]
Ag NPs@SCOF	50	3 min	17.6×10^{-2}		81	[61]
Ag@CMP	7.4	1 h	0.135×10^{-2}	1.84	17	[62]
Cu/AgNSs	0.0075	6 min	0.53×10^{-2}		720	[63]
AgNDs	0.054	8 min	0.21×10^{-2}		25.8	[64]
HPGNPs		9 min	0.747×10^{-2}		94	[65]
PCB-AgNPs		60 s	0.43×10^{-2}	10.617		[66]
Ag/C spheres	1	25 min	0.17×10^{-2}	0.331		[67]
Ag/nanodendrites		600 s	0.56×10^{-2}	0.304		[68]
Ag/nanosilica	2	78 min	0.076×10^{-2}	1.130		[69]
0.5%Au/PDA (Sol)	5	240 s	0.973×10^{-2}		10,125	[70]
$AuNPs/Al_2O_3$	2	12 min	0.46×10^{-2}			[71]
Al_2O_3/Ag	10	120 s	3.535×10^{-2}			[72]
AgNSs-DP20	0.02	6 min	1.196×10^{-2}			[73]
FeNi@NPG-0.08	0.3	180 s	0.49×10^{-2}			[74]

2.2.3. Mechanistic Insight: Correlating Electronic Structure with Activity

The superior performance of the AgFe-0.4 catalyst cannot be explained by porosity alone. The lower activity of the similarly porous AgFe-0.6 and Janus structure points to an additional electronic factor. Our XPS analysis provides direct evidence for this: the observed charge transfer from Ag to Fe_3O_4 (Figure 5) is most favorable in the AgFe-0.4 sample. This electron donation creates d-hole vacancies on the Ag surface, enhancing the adsorption of H^- intermediates and thereby accelerating the catalytic kinetics, consistent with the Langmuir–Hinshelwood mechanism depicted in Figure 7 [5,75].

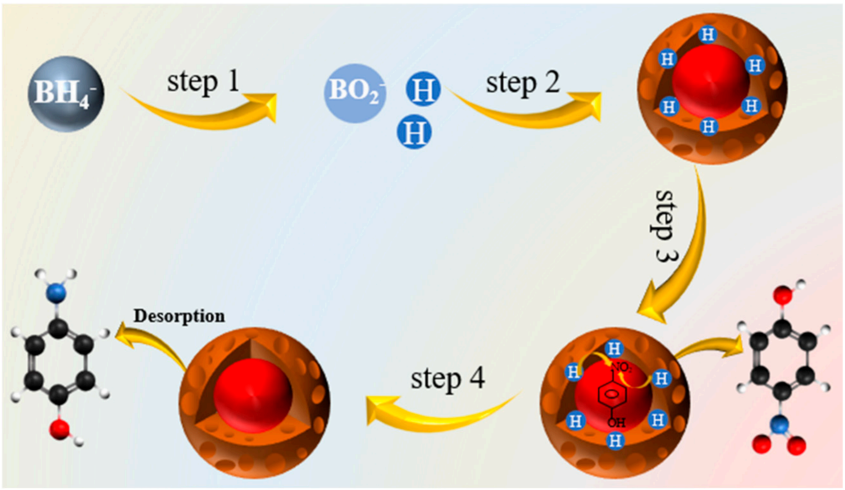

Figure 7. The proposed reaction mechanism for the catalytic reduction of 4-NP.

2.2.4. Magnetic Properties and Recyclability

The practical utility of the optimal AgFe-0.4 catalyst was demonstrated through its excellent recyclability. The nanocomposite exhibited superparamagnetic behavior (Figure 8A) with a saturation magnetization of 48.6 emu/g, enabling rapid magnetic separation within one minute (Figure 8B). Over eight consecutive cycles, the catalyst maintained a conversion efficiency of >95% without significant deactivation (Figures 8C and S4). After being repeated eight times, AgFe-0.4 nanocomposites maintained good morphology and structure, a shown in Figure 8D.

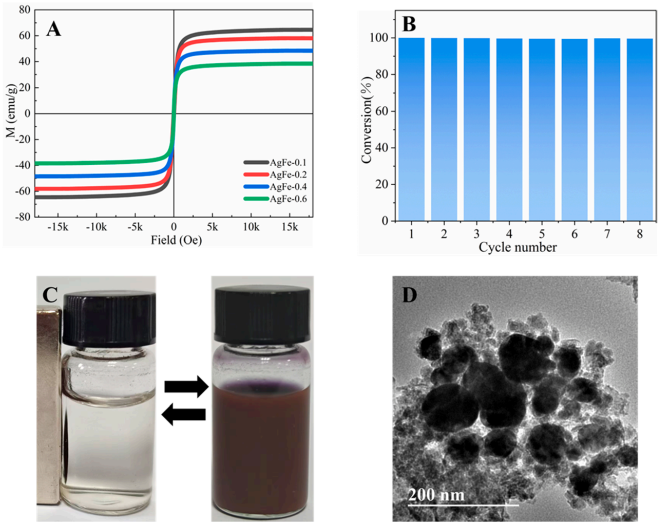

Figure 8. (**A**) Field-dependent magnetization curves of Ag/Fe_3O_4 magnetic nanocomposites at 300 K, (**B**) The enrichment and redispersion process of porous AgFe-0.4 magnetic nanocomposites, (**C**) The reusability of porous AgFe-0.4 magnetic nanocomposites, and (**D**) TEM images porous AgFe-0.4 magnetic nanocomposites after 8 times repeatability tests.

2.2.5. Catalytic Performance of Porous Ag@Fe_3O_4 Magnetic Nanoreactors for Hydrogenation of Different Nitroaromatics

To verify the prepared porous Ag@Fe_3O_4 magnetic nanoreactors with generality and robustness, we investigated the catalytic reduction of nitroaromatics bearing different functional groups. Nitrobenzene, p-NT (with methyl group), p-NCB (with halogen), p-NAN (with amino group), and 6-NPI (heterocyclic ring compound) were used as substrate to characterize the catalytic properties, as shown in Figures 9 and S5. The catalytic performance for different nitroaromatics were listed in Table 3. For all substrates, the reduction reaction completed within 3 min. All the conversion efficiency were above 95%. The hydrogenation of different nitroaromatics exhibited high-rate constants.

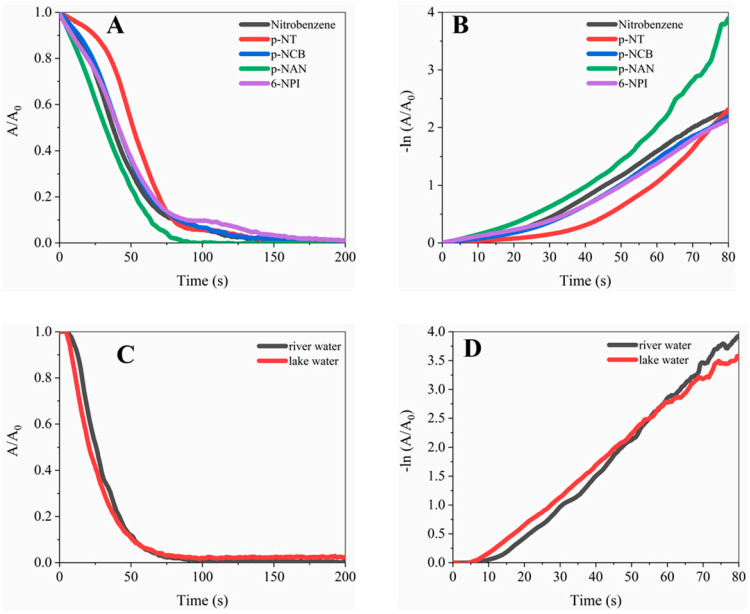

Figure 9. Catalytic performance of porous Ag@Fe_3O_4 magnetic nanoreactors for the reduction of different Nitroaromatics (**A**,**B**) and for reduction 4-NP in river water and lake water (**C**,**D**): (**A**,**C**) Normalized A_t/A_0 versus reaction time, (**B**) Pseudo-first-order kinetic plots derived from the date in (**A**), and (**D**) Pseudo-first-order kinetic plots derived from the date in (**C**).

Table 3. Catalytic properties of porous Ag@Fe_3O_4 magnetic nanoreactors in the $NaBH_4$-mediated hydrogenation reduction of different nitroaromatics.

Substrate	Substrate	Product	Reaction Time (s)	Conv. [%]	k (s^{-1})
Nitrobenzene	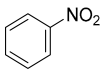	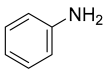	95	95	3.16×10^{-2}
p-NT	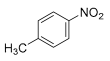	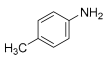	100	95	2.69×10^{-2}
p-NCB	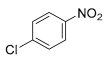	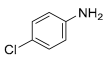	120	95	2.94×10^{-2}
p-NAN	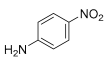	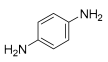	85	95	4.47×10^{-2}
6-NPI	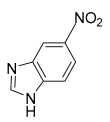	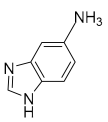	150	95	2.79×10^{-2}

2.2.6. Catalytic Performance of Porous Ag@Fe_3O_4 Magnetic Nanoreactors for Reduction 4-NP in Natural Environments

To verify the prepared porous Ag@Fe_3O_4 magnetic nanoreactors with real application in environment governance, we investigated the catalytic reduction of 4-NP in natural aqueous solution. As shown in Figure 9C,D, the porous Ag@Fe_3O_4 magnetic nanoreactors in river water and lake water remains good catalytic performance towards the reduction of 4-NP. The reduction reaction completed within 100 s. The conversion efficiencies were above 95%. The catalytic rate constants were 5.51×10^{-2} s^{-1} (in river water) and 4.98×10^{-2} s^{-1} (in lake water) in Table 4, respectively. In our experiment, the chemical composition of natural water was not analyzed. Ions (Na^+, K^+, Ca^{2+}, Mg^{2+}, Cl^-, $SO_4{}^{2-}$, or others) present in natural water could potentially affect the degradation reaction of 4-NP, but this is not the focus of our article. The porous Ag@Fe_3O_4 magnetic nanoreactors in river water and lake water remained good catalytic performance towards the reduction of 4-NP. These catalytic results confirm the practical applicability of our catalyst in real environmental samples.

Table 4. Catalytic hydrogenation of 4-NP by porous Ag@Fe_3O_4 magnetic nanoreactors in natural environments.

Solution	Reaction Time (s)	Conv. [%]	k (s^{-1})
river water	105	95	5.51×10^{-2}
lake water	100	95	4.98×10^{-2}

3. Materials and Methods

3.1. Materials

The following analytical grade reagents were used as received: Iron (III) nitrate nonahydrate ($Fe(NO_3)_3{\cdot}9H_2O$), silver nitrate ($AgNO_3$), sodium borohydride ($NaBH_4$), ethylene glycol (EG), anhydrous sodium acetate (NaOAc), and ethanol (Sinopharm Chemical Reagent Co., Ltd., Shanghai, China). Nitrobenzene, 4-nitrophenol (4-NP), p-nitroaniline (p-NAN), and 6-nitrobenzimidazole (6-NPI) were obtained from Aladdin Co. p-Nitrotoluene (p-NT) and p-nitrochlorobenzene (p-NCB) were purchased from Shanghai Macklin Biochemical Co., Ltd., Shanghai, China. All experiments utilized ultrapure water (18.2 MΩ·cm). Before use, all glassware was meticulously cleaned with freshly prepared aqua regia (HCl:HNO_3, 3:1 v/v) and rinsed with ultrapure water.

3.2. Preparation of Ag/Fe_3O_4 Nanocomposites

Ag/Fe_3O_4 nanocomposites with tunable morphologies were synthesized via a modified one-step polyol method [41,76]. In a representative procedure for synthesizing the porous AgFe-0.4 nanocomposite, $AgNO_3$ (0.0459 g), and $Fe(NO_3)_3{\cdot}9H_2O$ (1.0908 g) were dissolved in 30 mL of EG under vigorous stirring at 600 rpm to form a clear, homogeneous solution. Subsequently, sodium acetate (1.8 g) was added as an alkaline mineralizer and electrostatic stabilizer. After stirring for 30 min, the resulting suspension was transferred to a 100 mL Teflon-lined stainless-steel autoclave and heated at 200 °C for 7 h to facilitate simultaneous reduction and nucleation processes.

After the autoclave cooled to room temperature naturally, the black magnetic product was collected using an external magnet. The product was then washed sequentially with anhydrous ethanol and ultrapure water (three times each) to remove residual organics and salts. Finally, the product was divided into two portions: one was dried under vacuum at room temperature for 24 h to obtain a black powder for solid-state characterization, and the

other was redispersed in ultrapure water to form a stable colloidal suspension (0.1 mg/mL) for catalytic tests.

To investigate the effect of composition on morphology, the Ag:Fe molar ratio was systematically varied while keeping the total reaction volume and Fe precursor concentration constant. The corresponding samples are denoted as AgFe-0.1, AgFe-0.2, AgFe-0.4, and AgFe-0.6, where the number indicates the nominal Ag:Fe molar ratio.

3.3. Evaluation of Catalytic Performance

The catalytic performance of the Ag/Fe_3O_4 nanocomposites was evaluated using the benchmark reduction of 4-NP to 4-AP by $NaBH_4$ in aqueous solution [57,58]. A standard catalytic test was conducted as follows: first, 50 μL of the catalyst colloidal suspension (0.1 mg mL^{-1}) was mixed with 2.57 mL of ultrapure water in a quartz cuvette. Then, 180 μL of an aqueous 4-NP solution (1.1 mM) was added, followed by the rapid injection of 200 μL of a freshly prepared $NaBH_4$ solution (0.4 M) to initiate the reaction. This resulted in a total reaction volume of 3.0 mL with final concentrations of approximately 1.67 μg mL^{-1} catalyst, 0.066 mM 4-NP, and 26.7 mM $NaBH_4$. All catalytic reactions were carried out at 25 °C. The reaction does not require stirring. The large excess of $NaBH_4$ relative to 4-NP ensured pseudo-first-order reaction kinetics with respect to 4-NP concentration.

The cuvette was immediately transferred to a UV-Vis spectrophotometer, and the temporal decay of the 4-nitrophenolate ion absorbance at 400 nm was monitored at room temperature (ca. 25 °C). For recyclability tests, the catalyst was magnetically separated after each reaction cycle, washed thoroughly with ultrapure water to remove any adsorbed reactants or products, and then redispersed in a fresh reaction mixture to start the next cycle under identical conditions.

During catalytic reduction of 4-NP in natural aqueous solution experiments, the step was same except that the river water and lake water were used. The river water used in our study was collected from Benghe River (Linyi section, China, 35°08′01″ N, 118°17′15″ E). The Lake water was collected from Litter Lake in Linyi University (35°07′17″ N, 118°16′38″ E). The collected natural water was filtered through a 200 nm filter membrane and spiked with 4-NP to simulate contamination.

3.4. Characterization

The synthesized nanocomposites were characterized to determine their structural, compositional, optical, and magnetic properties. The crystalline structure and phase composition were analyzed using X-ray diffraction (XRD) on a Rigaku SmartLab3000 diffractometer (Rigaku Holdings Corporation, Tokyo, Japan). Morphology, size, and elemental composition were investigated using a JEM-2100 transmission electron microscope (JEOL Ltd., Tokyo, Japan) operated at 200 kV, equipped with an energy-dispersive X-ray spectroscopy (EDS) detector; particle size distributions were statistically determined from over 100 individual particles in TEM images. Morphology, size, and elemental composition were also investigated using a FE-SEM-5000 scanning electron microscope (CIQTEK, Hefei, China) equipped with an energy-dispersive X-ray spectroscopy (EDS) detector. Surface chemical states were probed by X-ray photoelectron spectroscopy (XPS) on a Thermo Fisher ESCALAB Xi+ system with an Al Kα X-ray source (1486.6 eV), and all binding energies were referenced to the C 1 s peak at 284.8 eV. Quantitative elemental analysis of silver and iron was performed by inductively coupled plasma optical emission spectrometry (ICP-OES) using an EXPEC6000 instrument. Optical properties, including extinction spectra and time-dependent absorbance during catalytic reactions, were recorded with a Shimadzu UV-3600 UV-Vis spectrophotometer. Magnetic properties were measured at

300 K using a LakeShore 7404 vibrating sample magnetometer (VSM), with magnetization curves collected between −20 kOe and +20 kOe. Finally, textural properties were assessed from nitrogen adsorption–desorption isotherms measured at 77 K on a Quantachrome NOVAtouch LX3 analyzer (Anton Paar, Austria), with the specific surface area calculated using the Brunauer–Emmett–Teller (BET) method.

4. Conclusions

In summary, this work demonstrates Ag@Fe_3O_4 nanocomposites were controllably synthesized by a facile one-pot polyol method. By varying the Ag:Fe precursor ratio, the structure could be tuned from dense and porous core-shell to Janus architectures. The porous Ag@Fe_3O_4 nanoreactors (Ag:Fe-0.4) exhibited exceptional catalytic performance, achieving complete 4-NP reduction within 75 s, with an apparent rate constant (k) of 6.29×10^{-2} s^{-1}, a normalized rate constant (k_n) of 3742 s^{-1} $mmol^{-1}$, and a TOF value of 1042 h^{-1}. XPS results verified that the excellent activity originated from the porous structure and interfacial charge transfer from Ag to Fe_3O_4. The catalysts showed superparamagnetism and could be reused for at least eight cycles with >95% conversion retained. It also displayed high efficiency in reducing diverse nitroaromatics and in natural water. This work highlights the significance of structural and electronic modulation, providing a scalable strategy for magnetically recyclable catalysts toward environmental remediation and heterogeneous catalysis.

Supplementary Materials: The following supporting information can be downloaded at https://www.mdpi.com/article/10.3390/catal16050445/s1: Figure S1. The size distribution of Ag/Fe_3O_4 magnetic nanocomposites (A, B, C, D) and Ag core (E, F, G, H). Figure S2. The EDS spectrum of Ag/Fe_3O_4 magnetic nanocomposite. (A) AgFe-0.1, (B) AgFe-0.2, (C) AgFe-0.4, and (D) AgFe-0.6. Figure S3. The UV-Vis spectral of Ag/Fe_3O_4 magnetic nanocomposite: (A) AgFe-0.1, (B) AgFe-0.2, (C) AgFe-0.4, and (D) AgFe-0.6. Figure S4. The UV-Vis spectra of 4-NP after reduction in different cycles. Figure S5. The adsorption spectra of nitrobenzene, p-nitroaniline (p-NAN), p-Nitrotoluene (p-NT) and p-nitrochlorobenzene (p-NCB) and 6-nitrobenzimidazole (6-NPI) before and after addition of NaBH4 solution. Table S1. Surface area, pore radius and total pore volume of Ag/Fe_3O_4 magnetic nanocomposites measured by BET.

Author Contributions: Methodology, Investigation, Formal Analysis, Writing Original Draft, S.S.; Investigation, Formal Analysis, C.L.; Writing—Review and Editing, S.M. and M.A.K.; Conceptualization, Funding Acquisition, Supervision, Writing—Review and Editing, F.Y. All authors have read and agreed to the published version of the manuscript.

Funding: The authors acknowledge the financial support from the Shandong Provincial Natural Science Foundation, China (ZR2022MB054, ZR2023MB155 and ZR2021MB133).

Data Availability Statement: All relevant data are available upon request of readers.

Acknowledgments: In the process of preparing this manuscript, we employed the AI tool DeepSeek. (web version, available at https://chat.deepseek.com/) specifically for polishing and refining the language of certain sentences on 21 April 2026. We also thank Tong Cui and Lei Wang (Qingdao University of Science & Technology) for their kind assistance with the XPS analysis.

Conflicts of Interest: The authors declare no conflicts of interest.

References

1. Fu, Y.; Qin, L.; Huang, D.; Zeng, G.; Lai, C.; Li, B.; He, J.; Yi, H.; Zhang, M.; Cheng, M.; et al. Chitosan functionalized activated coke for Au nanoparticles anchoring: Green synthesis and catalytic activities in hydrogenation of nitrophenols and azo dyes. *Appl. Catal. B Environ.* **2019**, *255*, 117740. [CrossRef]

2. Yang, C.; Yuan, W.; Liao, G.; Tang, Z.; Zhu, T.; Jia, Y.; Yu, Q.; Wang, L. Customized Vascular Repair Microenvironment: Poly(lactic acid)-Gelatin Nanofibrous Scaffold Decorated with bFGF and Ag@Fe(3)O(4) Core-Shell Nanowires. *ACS Appl. Mater. Interfaces* **2024**, *16*, 40787–40804. [CrossRef]
3. Zeng, J.; Zhang, Q.; Chen, J.; Xia, Y. A comparison study of the catalytic properties of Au-based nanocages, nanoboxes, and nanoparticles. *Nano Lett.* **2010**, *10*, 30–35. [CrossRef]
4. Lin, F.-h.; Doong, R.-a. Catalytic Nanoreactors of Au@Fe_3O_4 Yolk–Shell Nanostructures with Various Au Sizes for Efficient Nitroarene Reduction. *J. Phys. Chem. C* **2017**, *121*, 7844–7853. [CrossRef]
5. Wang, P.; Li, D.; Wang, L.; Guo, S.; Zhao, Y.; Shang, H.; Wang, D.; Zhang, B. Ultrafine CoNi alloy nanoparticles anchored on surface-roughened halloysite nanotubes for highly efficient catalytic hydrogenation of 4-nitrophenol. *Chem. Eng. J.* **2024**, *495*, 153631. [CrossRef]
6. Epa, U. Priority pollutant list. *Fed. Regist.* **1979**, *44*, 69514–69517.
7. Mörk, A.-K.; Malkiewicz, K.; Feng, M.C.; Silins, I. Proactive measures help shape the EU candidate list of substances of very high concern. *Nat. Commun.* **2025**, *16*, 4894. [CrossRef] [PubMed]
8. Ji, Y.; Shi, Y.; Yang, Y.; Yang, P.; Wang, L.; Lu, J.; Li, J.; Zhou, L.; Ferronato, C.; Chovelon, J.-M. Rethinking sulfate radical-based oxidation of nitrophenols: Formation of toxic polynitrophenols, nitrated biphenyls and diphenyl ethers. *J. Hazard. Mater.* **2019**, *361*, 152–161. [CrossRef]
9. Feng, C.; Wang, Y.; Xu, J.; Zheng, Y.; Zhou, W.; Wang, Y.; Luo, C. Precisely Tailoring Molecular Structure of Doxorubicin Prodrugs to Enable Stable Nanoassembly, Rapid Activation, and Potent Antitumor Effect. *Pharmaceutics* **2024**, *16*, 1582. [CrossRef]
10. Li, W.-Q.; Wu, J.-Y.; Xiang, D.-X.; Luo, S.-L.; Hu, X.-B.; Tang, T.-T.; Sun, T.-L.; Liu, X.-Y. Micelles loaded with puerarin and modified with triphenylphosphonium cation possess mitochondrial targeting and demonstrate enhanced protective effect against isoprenaline-induced H9c2 cells apoptosis. *Int. J. Nanomed.* **2019**, *14*, 8345–8360. [CrossRef]
11. Schug, T.T.; Janesick, A.; Blumberg, B.; Heindel, J.J. Endocrine disrupting chemicals and disease susceptibility. *J. Steroid Biochem. Mol. Biol.* **2011**, *127*, 204–215. [CrossRef]
12. Xu, J.; Wang, Y.; Zhao, W.; Han, L.; Tam, K.C. A novel magnetic cluster modified palladium-cellulose nanocrystal hybrids as recyclable catalyst for 4-nitrophenol reduction. *Mater. Today Commun.* **2022**, *33*, 104349. [CrossRef]
13. Tian, G.; Wang, Z.; Zhang, C.; Wei, F. Nano Bifunctional Catalysts as Miniaturized Chemical Processes for CO x-to-Aromatics Conversion. *Acc. Chem. Res.* **2026**, *59*, 646–658. [CrossRef] [PubMed]
14. Li, Y.; Bu, J.; Sun, Y.; Huang, Z.; Zhu, X.; Li, S.; Chen, P.; Tang, Y.; He, G.; Zhong, S. Efficient degradation of norfloxacin by synergistic activation of PMS with a three-dimensional electrocatalytic system based on Cu-MOF. *Sep. Purif. Technol.* **2025**, *356*, 129945. [CrossRef]
15. Jiang, F.; Zhang, Y.; Xu, X.; Mao, Y.; Wang, M.; Yang, B.; Zhang, C.; Feng, X.; Meng, H.; Guo, F. Application of cysteine with Cu2+ to strengthen Fenton-based treatment of coking wastewater used ferric sludge as a source of iron catalyst: Cl-removal and Fe3+/Fe2+ cycling. *J. Environ. Chem. Eng.* **2025**, *13*, 117556. [CrossRef]
16. Lan, D.; Zhu, H.; Zhang, J.; Li, S.; Chen, Q.; Wang, C.; Wu, T.; Xu, M. Adsorptive removal of organic dyes via porous materials for wastewater treatment in recent decades: A review on species, mechanisms and perspectives. *Chemosphere* **2022**, *293*, 133464. [CrossRef] [PubMed]
17. Donkadokula, N.Y.; Kola, A.K.; Naz, I.; Saroj, D. A review on advanced physico-chemical and biological textile dye wastewater treatment techniques. *Rev. Environ. Sci. Bio/Technol.* **2020**, *19*, 543–560. [CrossRef]
18. Yang, Y.; Jiang, K.; Guo, J.; Li, J.; Peng, X.; Hong, B.; Wang, X.; Ge, H. Facile fabrication of Au/Fe_3O_4 nanocomposites as excellent nanocatalyst for ultrafast recyclable reduction of 4-nitropheol. *Chem. Eng. J.* **2020**, *381*, 122596. [CrossRef]
19. Jiang, D.; Liu, F.; Yang, C.; Li, X.; Zhou, H.; Wang, H.; Qi, Z. Au/Ag synergistic catalysis of synthesis of 4 H-imidazo-oxadiazin-4-ones via three-component domino cyclization. *Org. Chem. Front.* **2025**, *12*, 5862–5867.
20. Nath, A.; Biswas, S.; Pal, P.; Pal, A. Reduction of 4-nitrophenol using copper loaded surfactant-modified chitosan beads: An approach towards sludge management. *Mater. Today Commun.* **2022**, *32*, 104044. [CrossRef]
21. Awad, A.M.; Shaikh, S.M.R.; Jalab, R.; Gulied, M.H.; Nasser, M.S.; Benamor, A.; Adham, S. Adsorption of organic pollutants by natural and modified clays: A comprehensive review. *Sep. Purif. Technol.* **2019**, *228*, 115719. [CrossRef]
22. Liao, G.; Gong, Y.; Zhong, L.; Fang, J.; Zhang, L.; Xu, Z.; Gao, H.; Fang, B. Unlocking the door to highly efficient Ag-based nanoparticles catalysts for NaBH4-assisted nitrophenol reduction. *Nano Res.* **2019**, *12*, 2407–2436. [CrossRef]
23. Ou, J.; Yu, S.; Liu, D.; Jiang, H.; Lyu, C.; Chen, K.; Li, J.; Yu, Z.; Liu, K.; Liu, J. Heterogeneous Fe single-atom catalysis for C2–H amidation of pyridine/quinoline N-oxides: Streamlined synthesis of pharmaceutical scaffolds. *Green Chem.* **2025**, *27*, 11882–11891. [CrossRef]
24. Ye, W.; Yu, J.; Zhou, Y.; Gao, D.; Wang, D.; Wang, C.; Xue, D. Green synthesis of Pt–Au dendrimer-like nanoparticles supported on polydopamine-functionalized graphene and their high performance toward 4- nitrophenol reduction. *Appl. Catal. B Environ.* **2016**, *181*, 371–378. [CrossRef]

25. Albukhari, S.M.; Ismail, M.; Akhtar, K.; Danish, E.Y. Catalytic reduction of nitrophenols and dyes using silver nanoparticles @ cellulose polymer paper for the resolution of waste water treatment challenges. *Colloids Surf. A Physicochem. Eng. Asp.* **2019**, *577*, 548–561. [CrossRef]
26. Jin, B.; Yan, F.; Qi, X.; Cai, B.; Tao, J.; Fu, X.; Tan, S.; Zhang, P.; Pfaendtner, J.; Naser, N.Y.; et al. Peptoid-Directed Formation of Five-Fold Twinned Au Nanostars through Particle Attachment and Facet Stabilization. *Angew. Chem. Int. Ed.* **2022**, *61*, e202201980. [CrossRef]
27. Yan, F.; Liu, L.; Walsh, T.R.; Gong, Y.; El-Khoury, P.Z.; Zhang, Y.; Zhu, Z.; De Yoreo, J.J.; Engelhard, M.H.; Zhang, X.; et al. Controlled synthesis of highly-branched plasmonic gold nanoparticles through peptoid engineering. *Nat. Commun.* **2018**, *9*, 2327. [CrossRef] [PubMed]
28. Ma, D.; Lu, H.; Zhou, Y.; Jiang, S.; Wang, D.; Yue, Q. A Novel Molten Salt Mediated Synthesis of Mesoporous Metal Oxides with High Crystallization. *ACS Cent. Sci.* **2024**, *10*, 676–683. [CrossRef]
29. Fang, Y.; Liu, Q.; Tian, M.; Ruan, L.; Chen, K.; Zhang, H.; Yang, Z.; Ye, H.; Zhu, L. Synergistic effect of Pt single atoms, clusters and nanoparticles on carbon doping with nitrogen for highly efficient and selective hydrogenation of nitroaromatics. *J. Mater. Chem. A* **2025**, *13*, 21971–21978. [CrossRef]
30. Ai, Y.; Hu, Z.; Liu, L.; Zhou, J.; Long, Y.; Li, J.; Ding, M.; Sun, H.-B.; Liang, Q. Magnetically Hollow Pt Nanocages with Ultrathin Walls as a Highly Integrated Nanoreactor for Catalytic Transfer Hydrogenation Reaction. *Adv. Sci.* **2019**, *6*, 1802132. [CrossRef]
31. Shaban, S.M.; Kim, S.; Basiony, N.M.E.; Kappen, J.; Mostafa, M.H.; Elbalaawy, A.Y.; Elmasry, M.R.; Shin, J.; Jeon, I.; Kim, D.-H. Ecofriendly Sunlight-Mediated Nontoxic Bimetallic Nanoparticles: Synthesis, Reusable Catalytic Membrane, and Biosensor Applications. *Adv. Sci.* **2025**, *12*, 2503120. [CrossRef]
32. Krishna, R.; Fernandes, D.M.; Dias, C.; Ventura, J.; Venkata Ramana, E.; Freire, C.; Titus, E. Novel synthesis of Ag@Co/RGO nanocomposite and its high catalytic activity towards hydrogenation of 4-nitrophenol to 4-aminophenol. *Int. J. Hydrogen Energy* **2015**, *40*, 4996–5005. [CrossRef]
33. Lv, Z.-S.; Zhu, X.-Y.; Meng, H.-B.; Feng, J.-J.; Wang, A.-J. One-pot synthesis of highly branched Pt@Ag core-shell nanoparticles as a recyclable catalyst with dramatically boosting the catalytic performance for 4-nitrophenol reduction. *J. Colloid Interface Sci.* **2019**, *538*, 349–356. [CrossRef]
34. Triviño-Sánchez, S.; Xu, R.; González-Izquierdo, J.; Bañares, L.; Cano, I.; Pérez-Juste, J.; Guerrero-Martínez, A.; González-Rubio, G. Colloidal gold-palladium-platinum alloy nanospheres with tunable compositions and defined numbers of atoms. *Nanoscale* **2025**, *17*, 8577–8587. [CrossRef]
35. Deng, Y.; Yuan, X.; Zhang, W.; Tang, J. Effective catalytic reduction of 4-nitrophenol by the prepared gold-palladium core-shell bimetallic nanostructures. *J. Mol. Struct.* **2026**, *1352*, 144578. [CrossRef]
36. Ruditskiy, A.; Xia, Y. Toward the Synthesis of Sub-15 nm Ag Nanocubes with Sharp Corners and Edges: The Roles of Heterogeneous Nucleation and Surface Capping. *J. Am. Chem. Soc.* **2016**, *138*, 3161–3167. [CrossRef] [PubMed]
37. Shi, Y.; Lyu, Z.; Zhao, M.; Chen, R.; Nguyen, Q.N.; Xia, Y. Noble-Metal Nanocrystals with Controlled Shapes for Catalytic and Electrocatalytic Applications. *Chem. Rev.* **2021**, *121*, 649–735. [CrossRef] [PubMed]
38. Hong, X.; Wang, D.; Cai, S.; Rong, H.; Li, Y. Single-Crystalline Octahedral Au–Ag Nanoframes. *J. Am. Chem. Soc.* **2012**, *134*, 18165–18168. [CrossRef] [PubMed]
39. Zou, Y.; Sun, Z.; Wang, Q.; Ju, Y.; Sun, N.; Yue, Q.; Deng, Y.; Liu, S.; Yang, S.; Wang, Z.; et al. Core–Shell Magnetic Particles: Tailored Synthesis and Applications. *Chem. Rev.* **2025**, *125*, 972–1048. [CrossRef] [PubMed]
40. Das, R.; Sypu, V.S.; Paumo, H.K.; Bhaumik, M.; Maharaj, V.; Maity, A. Silver decorated magnetic nanocomposite (Fe_3O_4@PPy-MAA/Ag) as highly active catalyst towards reduction of 4-nitrophenol and toxic organic dyes. *Appl. Catal. B Environ.* **2019**, *244*, 546–558. [CrossRef]
41. Jiang, T.; Wang, Z.; Luo, Z.; He, J.; Hu, C.; Xiang, X.; Cao, Y.; Fang, G.; Peng, K.; Liu, C. Constructing heterogeneous conductive network with core-shell Ag@Fe_3O_4 for dual-band effective microwave absorption. *Appl. Surf. Sci.* **2023**, *610*, 155231. [CrossRef]
42. Wang, R.; Cai, C.; Wang, D.; Liu, Z.; Gao, L.; Jiao, T. Self-assembled Au/Fe_3O_4 nanoparticle-loaded phytic acid-graphene oxide composite foam with highly efficient catalytic performance for p-nitrophenol and o-nitroaniline organic pollutants. *Colloids Surf. A Physicochem. Eng. Asp.* **2021**, *617*, 126368. [CrossRef]
43. Yu, J.; Zhu, D.; Qi, C.; Zhang, W.; Liang, L. Controllable preparation of Ag@Fe_3O_4 core-shell nanoparticles and evaporation characteristics of nanoparticles-modified carbon membranes. *Colloids Surf. A Physicochem. Eng. Asp.* **2024**, *687*, 133598. [CrossRef]
44. Gabbani, A.; Fantechi, E.; Petrucci, G.; Campo, G.; de Julián Fernández, C.; Ghigna, P.; Sorace, L.; Bonanni, V.; Gurioli, M.; Sangregorio, C.; et al. Dielectric Effects in FeOx-Coated Au Nanoparticles Boost the Magnetoplasmonic Response: Implications for Active Plasmonic Devices. *ACS Appl. Nano Mater.* **2021**, *4*, 1057–1066. [CrossRef]
45. Xu, Z.; Hou, Y.; Sun, S. Magnetic Core/Shell Fe_3O_4/Au and Fe_3O_4/Au/Ag Nanoparticles with Tunable Plasmonic Properties. *J. Am. Chem. Soc.* **2007**, *129*, 8698–8699. [CrossRef]

46. Oliveira-Filho, G.B.; Atoche-Medrano, J.J.; Aragón, F.F.H.; Mantilla Ochoa, J.C.; Pacheco-Salazar, D.G.; da Silva, S.W.; Coaquira, J.A.H. Core-shell Au/Fe_3O_4 nanocomposite synthesized by thermal decomposition method: Structural, optical, and magnetic properties. *Appl. Surf. Sci.* **2021**, *563*, 150290. [CrossRef]
47. Lin, F.-h.; Doong, R.-a. Characterization of interfacially electronic structures of gold–magnetite heterostructures using X-ray absorption spectroscopy. *J. Colloid Interface Sci.* **2014**, *417*, 325–332. [CrossRef]
48. Kim, J.; Rong, C.; Lee, Y.; Liu, J.P.; Sun, S. From Core/Shell Structured FePt/Fe_3O_4/MgO to Ferromagnetic FePt Nanoparticles. *Chem. Mater.* **2008**, *20*, 7242–7245. [CrossRef]
49. Michałowska, A.; Żygieło, M.; Kudelski, A. Fe_3O_4-protected gold nanoparticles: New plasmonic-magnetic nanomaterial for Raman analysis of surfaces. *Appl. Surf. Sci.* **2021**, *562*, 150220. [CrossRef]
50. Chakraborty, I.; Bose, S.; Chatterjee, K. Designer Fe_3O_4@Ag Core–Shell Porous Nanospheres for Enhanced Electromagnetic Interference Shielding of Polymer Nanocomposites. *Adv. Eng. Mater.* **2023**, *25*, 2201363. [CrossRef]
51. Zhang, Y.; Ding, H.; Liu, Y.; Pan, S.; Luo, Y.; Li, G. Facile one-step synthesis of plasmonic/magnetic core/shell nanostructures and their multifunctionality. *J. Mater. Chem.* **2012**, *22*, 10779–10786. [CrossRef]
52. Kang, Z.; Zhu, S.; Wang, S.; Xiang, Z.; Deng, Z.; Tong, X.; Wang, Z.; Sun, Y.; Liu, X.; Zang, G. Precision-Engineered Co-N4− x-C x Single Atoms Enhance Potential-Resolved Ru (bpy) 32+ Electrochemiluminescence via Reactive Oxygen Species. *Research* **2025**, *8*, 0842. [CrossRef] [PubMed]
53. Zhai, Y.; Han, L.; Wang, P.; Li, G.; Ren, W.; Liu, L.; Wang, E.; Dong, S. Superparamagnetic plasmonic nanohybrids: Shape-controlled synthesis, TEM-induced structure evolution, and efficient sunlight-driven inactivation of bacteria. *ACS Nano* **2011**, *5*, 8562–8570. [CrossRef]
54. Guo, S.; Li, D.; Zhang, L.; Li, J.; Wang, E. Monodisperse mesoporous superparamagnetic single-crystal magnetite nanoparticles for drug delivery. *Biomaterials* **2009**, *30*, 1881–1889. [CrossRef]
55. Zhan, Z.; Zhang, J.; Lin, L.; Jiang, T.; Shi, J. Salt-templated two-step activation synthesis of poplar-derived hierarchical porous carbon for high-performance supercapacitor electrodes. *Ind. Crops Prod.* **2025**, *236*, 122105. [CrossRef]
56. Li, L.; Liu, Y.; Gui, X.; Zhou, B.; Xing, Z.; Ke, X.; Yuan, J.; Zhao, T. Size-dependent regulation of iron transport and nitrogen metabolism by nanoscale zero-valent iron in heterotrophic nitrifying–aerobic denitrifying bacteria. *Bioresour. Technol.* **2026**, *449*, 134383. [CrossRef] [PubMed]
57. Yan, F.; Hu, Z.; Tian, Q.; Wang, B. Facile synthesis of porous hollow Au nanoshells with enhanced catalytic properties towards reduction of p-nitrophenol. *Inorg. Chem. Commun.* **2020**, *116*, 107896. [CrossRef]
58. Yan, F.; Sun, R. Facile synthesis of bifunctional Fe_3O_4/Au nanocomposite and their application in catalytic reduction of 4-nitrophenol. *Mater. Res. Bull.* **2014**, *57*, 293–299. [CrossRef]
59. Mao, H.; Ji, C.; Liu, M.; Cao, Z.; Sun, D.; Xing, Z.; Chen, X.; Zhang, Y.; Song, X.-M. Enhanced catalytic activity of Ag nanoparticles supported on polyacrylamide/polypyrrole/graphene oxide nanosheets for the reduction of 4-nitrophenol. *Appl. Surf. Sci.* **2018**, *434*, 522–533. [CrossRef]
60. Hareesh, K.; Joshi, R.P.; Sunitha, D.V.; Bhoraskar, V.N.; Dhole, S.D. Anchoring of Ag-Au alloy nanoparticles on reduced graphene oxide sheets for the reduction of 4-nitrophenol. *Appl. Surf. Sci.* **2016**, *389*, 1050–1055. [CrossRef]
61. Wang, N.; Wang, F.; Pan, F.; Yu, S.; Pan, D. Highly Efficient Silver Catalyst Supported by a Spherical Covalent Organic Framework for the Continuous Reduction of 4-Nitrophenol. *ACS Appl. Mater. Interfaces* **2021**, *13*, 3209–3220. [CrossRef]
62. Cao, H.-L.; Huang, H.-B.; Chen, Z.; Karadeniz, B.; Lü, J.; Cao, R. Ultrafine Silver Nanoparticles Supported on a Conjugated Microporous Polymer as High-Performance Nanocatalysts for Nitrophenol Reduction. *ACS Appl. Mater. Interfaces* **2017**, *9*, 5231–5236. [CrossRef]
63. Chen, J.; He, L.; Shen, B.; Yang, H.; Mao, H.; Ren, Y.; Yin, J.; Dai, W.; Zhao, S.; Chen, L.; et al. Ethanolamine-Induced Synthesis of Sesame Cake-like Cu/Ag Nanosheets with High Activity for the Reduction of p-Nitrophenol to p-Aminophenol. *ACS Appl. Nano Mater.* **2023**, *6*, 10494–10500. [CrossRef]
64. Chen, J.; He, L.; Fan, Z.; Yang, H.; Mao, H.; Ren, Y.; Yin, J.; Dai, W.; Cui, H. Ferric Chloride-Induced Synthesis of Silver Nanodisks with Considerable Activity for the Reduction of 4-Nitrophenol. *ACS Omega* **2022**, *7*, 28860–28865. [CrossRef] [PubMed]
65. Guo, M.; He, J.; Li, Y.; Ma, S.; Sun, X. One-step synthesis of hollow porous gold nanoparticles with tunable particle size for the reduction of 4-nitrophenol. *J. Hazard. Mater.* **2016**, *310*, 89–97. [CrossRef]
66. Song, J.; Zhu, Y.; Zhang, J.; Yang, J.; Du, Y.; Zheng, W.; Wen, C.; Zhang, Y.; Zhang, L. Encapsulation of AgNPs within Zwitterionic Hydrogels for Highly Efficient and Antifouling Catalysis in Biological Environments. *Langmuir* **2019**, *35*, 1563–1570. [CrossRef]
67. Tang, S.; Vongehr, S.; Meng, X. Carbon Spheres with Controllable Silver Nanoparticle Doping. *J. Phys. Chem. C* **2010**, *114*, 977–982. [CrossRef]
68. Zhang, W.; Tan, F.; Wang, W.; Qiu, X.; Qiao, X.; Chen, J. Facile, template-free synthesis of silver nanodendrites with high catalytic activity for the reduction of p-nitrophenol. *J. Hazard. Mater.* **2012**, *217–218*, 36–42. [CrossRef]
69. Das, S.K.; Khan, M.M.R.; Guha, A.K.; Naskar, N. Bio-inspired fabrication of silver nanoparticles on nanostructured silica: Characterization and application as a highly efficient hydrogenation catalyst. *Green Chem.* **2013**, *15*, 2548–2557. [CrossRef]

70. Sun, L.; Xie, Q.; Jing, H.; Liu, X.; Zhao, L.; Sun, X.; Duan, B.; Qi, C.; Su, H. A Comprehensive study on the reduction of 4-NP using Au/Polydopamine catalysts. *Appl. Surf. Sci.* **2025**, *680*, 161376. [CrossRef]
71. Xu, M.; Gong, Z.; Wu, Y.; Zhu, Z.; Wang, K.; Xu, H.; Yu, C.; Chu, X. Evaluation of Au Nanoparticle Catalysts Supported on Metal Oxide for the Catalytic Reduction of 4-NP. *Langmuir* **2025**, *41*, 17815–17828. [CrossRef]
72. Wang, H.; Dong, Y.; Xie, J.; Yuan, Y.; Yang, C.; He, S.; Liu, Y.; Lin, X.; Li, Y. Electronic Interface Interaction on Al2O3/Ag Inverse Catalysts for Enhanced Catalytic Reduction of 4-NP. *J. Phys. Chem. Lett.* **2026**, *17*, 1777–1785. [CrossRef]
73. Chen, Z.; Chen, J.; Mao, H.; Yin, J.; Ren, Y.; Dai, W.; Zhao, S.; Yang, H. Stacking faults-rich silver catalysts synthesized via self-assembly for the efficient catalytic reduction of nitrophenols/nitroanilines. *Appl. Surf. Sci.* **2026**, *729*, 166205. [CrossRef]
74. Xie, C.-Y.; Chen, Y.-S.; Tsai, M.-H.; Xie, B.-Y. Nitrogen-phosphorus dual-doped graphene-encapsulated magnetic Fe-Ni alloy nanoparticles/Au heterogeneous catalysts for the reduction of 4-nitrophenol. *J. Taiwan Inst. Chem. Eng.* **2026**, *187*, 106715. [CrossRef]
75. Cao, H.-L.; Liu, C.; Cai, F.-Y.; Qiao, X.-X.; Dichiara, A.B.; Tian, C.; Lü, J. In situ immobilization of ultra-fine Ag NPs onto magnetic Ag@RF@Fe_3O_4 core-satellite nanocomposites for the rapid catalytic reduction of nitrophenols. *Water Res.* **2020**, *179*, 115882. [CrossRef] [PubMed]
76. Jiang, W.; Zhou, Y.; Zhang, Y.; Xuan, S.; Gong, X. Superparamagnetic Ag@Fe_3O_4 core–shell nanospheres: Fabrication, characterization and application as reusable nanocatalysts. *Dalton Trans.* **2012**, *41*, 4594–4601. [CrossRef] [PubMed]